

A 170-GHz Fully Integrated Single-Chip FMCW Imaging Radar with 3-D Imaging Capability

Ali Mostajeran, *Student Member, IEEE*, Andreia Cathelin, *Senior Member, IEEE*,
and Ehsan Afshari, *Senior Member, IEEE*

Abstract—A 170-GHz fully integrated single-chip heterodyne frequency modulated continuous-wave (FMCW) imaging radar using a 130-nm SiGe BiCMOS technology ($f_T/f_{max} = 220/280$ GHz) is reported. This system demonstrates a wide bandwidth of 27.5 GHz (16.3%) at a center frequency of 168 GHz. A design methodology to maximize the tuning range of the voltage-controlled oscillator (VCO) is presented. A co-design of the VCO, coupler, and antenna is performed to minimize the chip area and the dc power consumption. The transmitter radiates a peak power of -1 dBm with a dc-to-RF efficiency of 1.42%. At the receiver side, a subharmonic mixer is used for signal down-conversion. The system achieves a measured sensitivity of 87 fW with a total dc power consumption of 67 mW. The prototype is capable of forming 2-D and 3-D images with a range resolution of 7 mm. To the best of our knowledge, this fully integrated imaging radar demonstrates the highest sensitivity and radiation efficiency among all imaging systems around 200 GHz. Moreover, the system is capable of practical 2-D and 3-D imaging with significantly lower dc power consumption compared to the state-of-the-art FMCW radars.

Index Terms—3-D imaging, antenna, coherent, detector, frequency modulated continuous wave (FMCW), hydration sensing, imager, imaging system, millimeter-wave (mm-wave), radar, sensitivity, subharmonic mixer, terahertz (THz) frequency, wideband voltage-controlled oscillator (VCO).

I. INTRODUCTION

RECENTLY there has been a significant interest in millimeter-wave (mm-wave)/terahertz (THz) imaging systems. These systems are used in different application areas such as biomedical imaging [1], [2], material analysis [3], quality control [3], and security [4]. THz radiation has several distinct advantages over other wavelengths of the electromagnetic (EM) spectrum. For instance, many dielectric materials are transparent to THz radiation. Unlike X-ray, THz radiation is nonionizing and consequently safe for biological tissues. Based on the Abbe diffraction limit at higher frequencies the beam waist of the illumination source becomes narrower. This results in high spatial resolution in the order of wavelength (~ 1 mm at around 300 GHz). In addition, the available

Manuscript received January 23, 2017; revised April 3, 2017, May 24, 2017, and July 3, 2017; accepted July 4, 2017. Date of publication August 4, 2017; date of current version September 21, 2017. This paper was approved by Associate Editor Wooguen Rhee. (Corresponding author: Ali Mostajeran.)

A. Mostajeran is with the Department of Electrical and Computer Engineering, Cornell University, Ithaca, NY 14853 USA, and also with the Department of Electrical and Computer Science, University of Michigan, Ann Arbor, MI 48109 USA (e-mail: am2457@cornell.edu).

A. Cathelin is with STMicroelectronics, 38920 Crolles, France.

E. Afshari is with the Department of Electrical and Computer Science, University of Michigan, Ann Arbor, MI 48109 USA.

Color versions of one or more of the figures in this paper are available online at <http://ieeexplore.ieee.org>.

Digital Object Identifier 10.1109/JSSC.2017.2725963

bandwidth is larger that results in higher range resolution [5]. Practical imaging systems at this frequency range mostly use off-chip components, which makes the system bulky and expensive [6]. Novel techniques are developed to generate reasonable amount of power at mm-wave/THz frequencies on silicon. Hence, a lot of effort has been made to implement fully integrated imaging systems [7]–[17]. A high integration level makes the system portable and decreases the overall cost.

In general, there are two types of active THz sensing modes: transmission and reflection. The advantage of transmission mode imagers is their simple design as only a single tone is transmitted. As a result, there is no need to deal with challenges of wideband voltage-controlled oscillator (VCO), antenna and matching network design. Successful works on transmission mode imaging are demonstrated in [7]–[13]. In [7], a 4×4 detector array is illuminated by a source array at 280 GHz. The detector outputs are sampled by a locked-in amplifier. However, due to the incoherent nature of the imaging scheme the sensitivity of the receiver (Rx.) is degraded and a minimum noise equivalent power of 7.9 pw/ $\sqrt{\text{Hz}}$ is achieved. This is also the case for the incoherent imager of [8] that is implemented at 530 GHz. As a result of incoherent nature of these imagers, a higher radiate power is required to obtain the minimum required SNR compared to the coherent cases. In [9] and [10], a fully integrated coherent imaging system at 320 GHz is demonstrated which the transmitter (Tx.) and Rx. frequencies are locked to off-chip low frequency references. Due to the coherent detection, a sensitivity of 70 pW is achieved. However, the performance of the system is limited by the uncorrelated phase noise of the VCOs at the Tx. and Rx. Hence, the IF level is only 5.5 dB larger than the output signal spectrum which is spread over the IF band. Moreover, all the transmission mode imagers are two chip solutions. This makes the imaging setup and arrangement of optical components more complicated. Furthermore, the transmission mode imagers do not provide the depth information.

The monostatic reflection mode imaging radar such as pulse-based or modulated continuous-wave radars are single-chip solutions [14]–[17]. It makes the system low cost while providing depth information for constructing 3-D images. However, it is at the expense of wideband VCO and antennas design challenges and dealing with Tx. to Rx. leakage. Pulse-based radars require fast and low-loss switches with high isolation level that is challenging to be implemented on chip at THz frequencies. Main drawback of the pulse-based radar is the challenges of baseband design and data processing due to its large baseband bandwidth. As an example in [14],

to capture a 36-ps pulsewidth [correspond to ~ 30 GHz of bandwidth (BW)] IF signal is probed and delivered to a wideband oscilloscope with a high sampling rate. On the other hand, continuous-wave imaging systems such as frequency modulated continuous-wave (FMCW) radars shows a superior performance for short-range applications. For FMCW radars, the IF frequency is typically in the order of tens to hundreds of kilohertz. It makes the baseband design and data processing simpler. However, the FMCW radars require a wide tuning range radiator that is challenging to be implemented on the silicon chip because of the limited range of the varactors [18]. At high frequencies, the varactor is lossy while its value is comparable with the parasitic capacitances, which limits the tuning range [19], [20]. Moreover, the FMCW radars suffer from Tx. to Rx. leakage. The fully integrated FMCW radar of [15] provides a radiation bandwidth of 15 GHz at a center frequency of 375 GHz. The system performance suffers from Tx. to Rx. leakage. In [16], an integrated multiplier chain ($\times 16$) is implemented that up-converts the chirp signal at 15 GHz generated off-chip. Using chain of multipliers and power amplifiers results in a large dc power consumption of around 2 W. Due to the high linearity of the off-chip chirp, a range resolution of 2.5 mm is achieved. In [17], a fully integrated FMCW radar with 40 GHz of bandwidth at a center frequency of 227 GHz is reported. The chirp is linearized inside a phase-locked loop (PLL), but due to large variation of IF level (due to variation of radiated power) the range resolution is degraded. In [17], after post signal processing a range resolution of 3.8 mm is achieved while the system consumes 3.5 W of dc power.

In this paper, we present a low power, fully integrated coherent FMCW imaging radar with >27 GHz of bandwidth at a center frequency of 168.2 GHz (16.3% tuning range). This system is capable of constructing 3-D images with 7 mm of depth resolution. The radiator provides a peak radiated power of -1 dBm and an effective isotropic radiated power (EIRP) of 16.2 dBm with a dc-to-RF efficiency of 1.42%. Using coherent subharmonic mixer at the Rx, a sensitivity of 87 fW is achieved. To the best of our knowledge, this work demonstrates the highest sensitivity and radiation efficiency among all imaging systems around 200 GHz. Moreover, the system is capable of practical 2-D and 3-D imaging with significantly lower dc power consumption compared to the state-of-the-art FMCW radars. The rest of the paper is organized as follows. In Section II, the link specifications for practical imaging is calculated. Besides, the impact of second-order effects such as nonlinearity of the chirp and the VCO phase noise on the system performance and the Tx. to Rx. leakage are discussed. The Tx. design including wideband VCO and antenna design is presented in Section III followed by the Rx. design in section IV. The experimental results of the SiGe prototype are presented in Section V. Finally, a performance comparison with state-of-the-arts concluded the paper in Section VI.

II. SYSTEM ANALYSIS

The system structure of an FMCW radar is demonstrated in Fig. 1. In the following, the required specifications of the

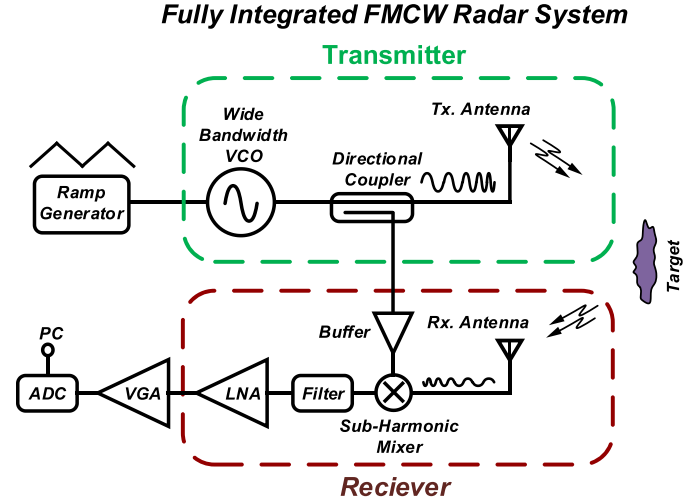


Fig. 1. Simplified system structure of an FMCW imaging radar.

transceiver link are calculated and second-order effects are discussed.

A. Link Budget Calculation

The minimum required radiated power is calculated based on the Rx. performance. According to simulated results of the Rx. (presented in Section IV), a Rx. sensitivity of -112 dBm is achieved. Here the sensitive is defined as the minimum received power (P_r) corresponding to an output SNR of 0 dB. Therefore, for an output SNR of more than 30 dB (typically good enough for imaging purposes), a minimum received power ($P_{r,\min}$) of -82 dBm is required. Using Friis equation, the minimum transmitted power ($P_{t,\min}$) is calculated by

$$P_{r,\min} = LP_{t,\min}G_t G_r \sigma \frac{\lambda^2}{(4\pi)^3 R^4} \quad (1)$$

where G_t and G_r are the gain of the Tx. and Rx. antennas, σ is the radar cross section (RCS) of the target, R is the stand-off distance, and λ is the wavelength of the radiated wave. In (1) the factor of L models the losses in the system such as dielectric loss, polarization mismatches of the radiated and received wave and reflection loss at the silicon-air boundary. For hydration sensing applications, the RCS might be as small as -30 dBsm [21]. Using (1), for a distance of $R = 20$ cm, $P_{t,\min} = -14$ dBm is required. The values for calculation of $P_{t,\min}$ are listed in TABLE I. Gain of each antenna is extracted from simulations that is discussed in the following sections. Assuming a safe margin of 4 dB, a radiated power of more than -10 dBm across the bandwidth is desired.

B. Range Resolution and Chirp Linearity

Range resolution (δ_r) of an imaging radar determines the minimum distance between two objects which can be resolved. It is related to the BW of the radiated signal as

$$\delta_r = \frac{c}{2\text{BW}} \quad (2)$$

TABLE I
VALUES USED TO CALCULATE THE MINIMUM
REQUIRED TRANSMITTED POWER

G_t	Tx. Antenna Gain	16.5 dBi
G_r	Rx. Antenna Gain	9.25 dBi
σ	Target RCS	-30dBsm
R	Range to target	20cm
λ	Wavelength	1.6mm
L	Dielectric Loss	3dB

where c is the speed of light. Therefore, for a targeted range resolution of 5 mm a chirp bandwidth of 30 GHz is required. Nonlinearity in the frequency of the chirp, spreads the baseband spectrum and degrades the range resolution. The chirp can be linearized inside a PLL [22], however implementation of wideband frequency dividers at THz frequencies is challenging [23] while they are power hungry. In another technique, based on the VCO frequency profile, the control voltage is swept nonlinearly to generate a linear chirp frequency [24]. Though the control waveform needs to be updated periodically due to the temperature variation and frequency pushing. The resolution in range can be recovered with post processing as well. Using signal-processing techniques, the chirp nonlinearity can be compensated. It is shown that the range resolution can be improved near to its theoretical limit [25]–[27]. In our design to decrease the complexity and lower the overall cost of the system, we compensate the chirp nonlinearity in digital domain.

C. VCO Phase Noise

The wideband high frequency VCOs suffer from high phase noise level due to the low quality factor of the varactors. In an imaging system the VCO phase noise is down converted to the IF band and increases the in-band noise level. Nonetheless, for short-range imaging radars, time of flight is significantly smaller than the noise correlation time at the desired offset frequency. As a result, the phase noise of the received signal is correlated with the phase noise of the LO which cancels out after down-conversion. In another word, considering phase noise of the transmitted signal as $L(f)$, the down converted in-band noise level at the IF can be expressed as [28]

$$L_{\text{IF}}(f) \propto L(f) \times \sin^2 \left(2\pi f_m \frac{R}{c} \right) \quad (3)$$

where f_m is the chirp rate (typically is in the order of a couple of kilohertz to tens of kilohertz). Therefore, for short distances, $\sin^2(2\pi f_m(R/c)) \sim 0$ and the effect of the phase noise is negligible.

D. Leakage

The performance of monostatic FMCW radars suffers from the Tx. to Rx. leakage [28]. In a conventional classical implementation of the radars, the low-noise amplifier (LNA) is the first block of the Rx. frontend. As a result, the leakage

of the Tx. signal can saturate the LNA and the Rx. frontend. Moreover, since the leaked signal has the same frequency as of the received signal it would be considered in-band and cannot be filtered out. Such systems are considered as interferer-limited systems. On the contrary, at THz and sub-THz frequencies implementation of LNA with a reasonable performance (in terms of noise figure, gain, and bandwidth) is challenging. Therefore, mixer first topologies should be implemented (Fig. 1). It is at the expense of the higher input noise level of the Rx. frontend, although we can solve the leakage problem. The leaked signal from Tx. to Rx., generates different components at the output of the down-conversion mixer at the IF. The first component is generated by the direct coupling of the Tx. and Rx. antennas on the chip. Due to the direct coupling of the Tx. and Rx. antennas, there is no time delay between the received wave at the Rx. antenna and the LO signal, therefore the leaked signal has the same frequency as the LO with just a phase difference. As a result, it only generates a dc component at the IF. This component is totally filtered by the dc decoupling capacitance of the following stage. The other leakage components at the IF are generated by the multi-reflection of the radiated wave at the silicon-air interface. However due to the small thickness of the silicon, the time of flight for the leakage would be considerably smaller compared to the time of flight for the wave which is reflected back from the object. As a result, after down-conversion at the IF, these components would fall in a much lower frequency compared to the frequency of interest and can be considered as out of band interferer at the IF. These components are attenuated by the high-pass filter followed by the mixer, as shown in Fig. 1. Consequently, the reflected wave from the object can be frequency resolved from the leakage. An LNA is implemented after the filter to make sure that the noise of the following stages does not contribute to the input noise level of the Rx. front. In such systems, the performance is limited by the input noise level of the mixer.

III. WIDE TUNING RANGE VCO DESIGN

On-chip power generation close to or beyond f_{max} is realized by two different schemes: frequency multipliers [29] and harmonic VCOs. The first method introduces a large power conversion loss. Hence, it mandates implementation of power hungry power amplifiers inside the multiplier chain to boost the power level [16]. It results in a larger silicon area and a higher dc power consumption. Moreover, inter-stage mismatches increase power variation across the bandwidth. For instance the $\times 16$ multiplier chain of [16], shows ~ 17 dB power variation across the chirp bandwidth. In [30], 39.3 GHz (20.7%) of bandwidth at a center frequency of 190.5 GHz is achieved by utilizing a band switching scheme. However, using multi-band signal sources for FMCW imaging radars is challenging, since the frequency and phase continuity and coherency of the signal may not be preserved within a chirp by switching between the bands. The structure of [30] shows more than 11 dB of power variation across its bandwidth. Variation of radiated power leads to broadening of the IF main lobe that degrades the range resolution [28], [31]. Alternatively,

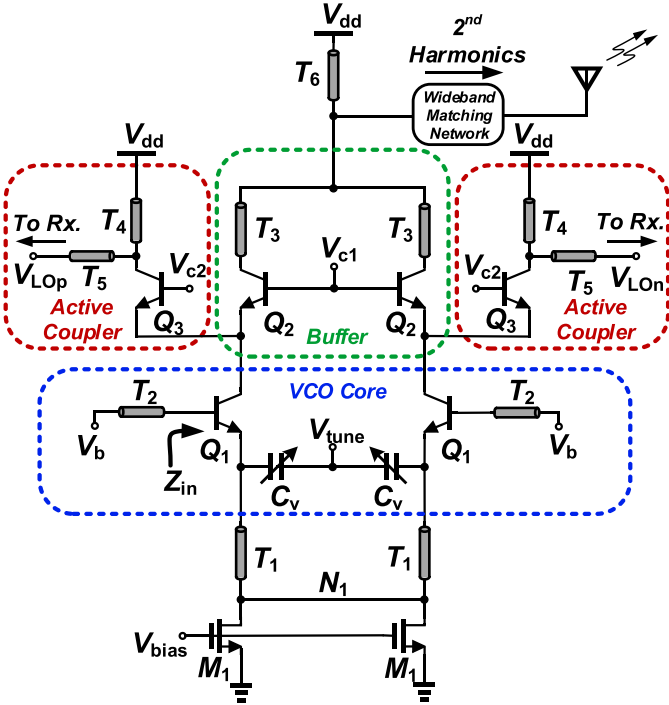


Fig. 2. Implemented wideband Colpitts structure integrated with buffer and the coupler.

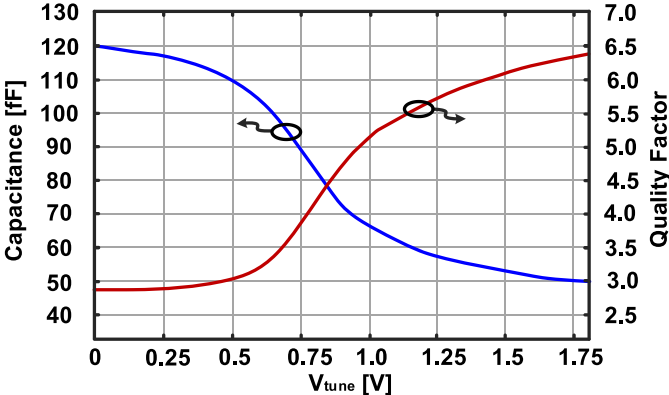


Fig. 3. $C - V$ curve of the varactor and the corresponding quality factor at 80 GHz.

harmonic VCOs are compact and power efficient with no inter-stage mismatch issue. As a result, the variation of radiated power can be minimized.

At mm-wave/THz frequencies Colpitts oscillator provides a wider tuning range compared to other commonly used topologies. It is because the contribution of the parasitic capacitance of the active devices to the tank is smaller [30], [32], [33]. Hence, differential Colpitts VCO of Fig. 2 is implemented for signal generation. A pair of varactors C_v is used for frequency tuning. The varactor size is chosen such that the minimum capacitance of the varactor is larger compared to the surrounding parasitic capacitances. As illustrated in Fig. 3, at 80 GHz, the varactors provide a $C_{\max}/C_{\min} \approx 120 \text{ fF}/50 \text{ fF}$ with a quality factor of 2.8–6.4 for a V_{tune} of 0–1.8 V. To determine the resonant frequency, core of the VCO and its small signal model are shown in Fig. 4. In Fig. 4, $-jX_E$

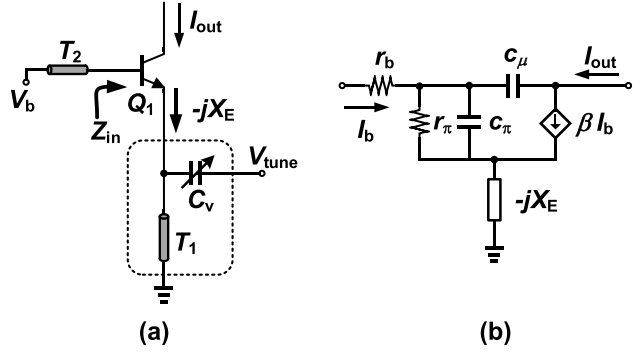


Fig. 4. Modeling the VCO core. (a) Simplified model of the VCO core for calculation of the resonance frequency. (b) Small signal model of the VCO core.

is the equivalent impedance at the emitter that for simplicity is assumed purely reactive. The input impedance at the base of Q_1 can be calculated as

$$Z_{\text{in}} = r_b + \frac{1}{j\omega C_{\pi}} + (1+\beta)(-jX_E) \quad (4)$$

where r_b is the base connection loss, C_{π} is the diffusion capacitance of Q_1 , and β is the ac current gain of the transistor.¹ In general β is a function of frequency and roll off by 10 dB/dec at a corner frequency of $\omega_B = 2\pi f_T/\beta_0$ which $f_T = g_m/(2\pi(C_{\pi} + C_{\mu}))$, f_T is the current gain cutoff frequency, g_m the trans-conductance of the transistor, C_{μ} the collector-base junction capacitance and β_0 is the dc current gain of the transistor [34]. At frequencies higher than ω_B , β is determined by

$$\beta = -j \frac{\omega_T}{\omega}. \quad (5)$$

Substituting (5) in (4), Z_{in} is calculated as

$$Z_{\text{in}} = r_b - \frac{\omega_T}{\omega} X_E - j \left(\frac{1}{C_{\pi}\omega} + X_E \right). \quad (6)$$

The real part is chosen to be negative to sustain the oscillation, while the reactive part resonates with transmission line T_2 to determine the oscillation frequency as

$$Z_{\text{in}} \tan(kl_2) = \frac{1}{C_{\pi}\omega} + X_E \quad (7)$$

where $k = \omega/v_{\text{TL}}$ is the wavenumber, v_{TL} is the wave speed inside the transmission line, and l_2 is the physical length of T_2 . In a conventional design, T_1 is chosen as a quarter wavelength transformer ($l_1 \approx \lambda/4$) [32], [33]. Hence, it introduces a high impedance at emitter of Q_1 , therefore $X_E = 1/C_{\pi}\omega$. The minimum oscillation frequency (ω_L) and maximum oscillation frequency (ω_H) can be calculated by substituting the corresponding $C_{v,\max}$ and $C_{v,\min}$ value in (7). Therefore, the tuning range is limited by the $C_{v,\max}/C_{v,\min}$ value that is reduced by the parasitic capacitances.

¹In this structure, the swing at the collector of the core transistor is relatively small since Q_2 and Q_3 provide a small impedance at this node. As a result, the effective value of the base-collector capacitance at the base is almost C_{μ} which $C_{\mu} \ll C_{\pi}$. Therefore, we can ignore C_{μ} in our calculations. We can also ignore the r_{π} compared to impedance of c_{π} , since at high frequencies $(r_{\pi}c_{\pi}\omega)^2 \gg 1$.

An optimum passive embedding around the core transistor can increase the tuning range. Considering length of T_1 as l_1 ($l_1 < \lambda/4$), X_E can be calculated as

$$X_E = \frac{1}{C_v \omega - 1/Z_0 \cot\left(\frac{\omega}{v_{TL}} l_1\right)}. \quad (8)$$

Substituting (8) in (7) the oscillation frequency is estimated by

$$Z_0 \tan(kl_2) = \frac{1}{C_\pi \omega} + \frac{Z_0 \tan(kl_1)}{Z_0 \omega C_v \tan(kl_1) - 1}. \quad (9)$$

By substituting $C_{v,\min}$ and $C_{v,\max}$ in (9), the tuning range can be calculated. It is possible to numerically maximize this tuning range by finding the optimum value of l_1 . This optimum value of l_1 can also be determined intuitively: the imaginary part of the base input impedance [the last term of right side of (6)] sets the oscillation frequency as given by (7). This term is mostly set by the value of X_E . Thus, to maximize the tuning range, the difference of X_E value for $V_{\text{tune},\min}$ and $V_{\text{tune},\max}$ should be maximized. X_E has some finite minimum value however its maximum could be quite large if the T_1 and C_v resonant at the frequency of interest, [ideally according to (8), X_E can becomes infinite, however in reality it is limited by the loss of T_1 and the varactors]. This resonance happens when this condition is satisfied

$$l_1 = \frac{v_{TL}}{\omega} \tan^{-1}\left(\frac{1}{Z_0 \omega C_v}\right). \quad (10)$$

Now the question is the values of C_v and ω in (10). To find the answer, we note that to sustain the oscillation, the real part of Z_{in} should be negative for the entire tuning range. According to (6), this means X_E has to be capacitive (i.e., $X_E > 0$) throughout the tuning range. To guarantee this, X_E should be capacitive for the minimum varactor value, $C_{v,\min}$. As a result we can make sure that the parallel combination of C_v and l_1 would be capacitive for larger values of C_v . This varactor value ($C_{v,\min}$) corresponds to the maximum oscillation frequency. To summarize, the optimum value of l_1 for a maximum tuning range is given by

$$l_{1,\text{opt}} = \frac{v_{TL}}{\omega_H} \tan^{-1}\left(\frac{1}{Z_0 \omega_H C_{v,\min}}\right). \quad (11)$$

In (11), the ω_H is chosen based on the device performance which could generated the desired power level at that frequency or can be chosen based on the system specifications. It should be considered that by choosing $l_1 < l_{1,\text{opt}}$, the X_E becomes inductive ($X_E < 0$) for $V_{\text{tune},\max}$, and there is no oscillation at the base for this tuning voltage. Therefore, in practice $l_1 \gtrsim l_{1,\text{opt}}$ is chosen.

For a designed value of $Z_0 = 50 \Omega$, $\omega_H = 90 \text{ GHz}$, and $C_{v,\min} = 50 \text{ fF}$, $l_{1,\text{opt}} \approx 165 \mu\text{m}$ is calculated from (11). To show the effectiveness of this optimization, we have simulated the Colpitts structure of Fig. 2 in a 130 nm SiGe process. The tuning bandwidth of the oscillator at the second harmonic as a function of l_1 is simulated and shown in Fig. 5. Based on the simulation results for $l_{1,\text{opt}} \approx 180 \mu\text{m}$ the tuning bandwidth is maximized and is significantly larger compared to the conventional design with $l_1 = \lambda/4 = 420 \mu\text{m}$.

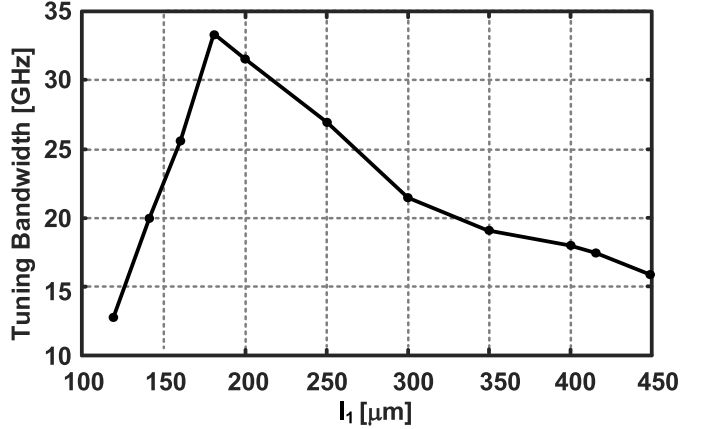


Fig. 5. Simulated tuning bandwidth of the VCO at the second harmonic as a function of l_1 .

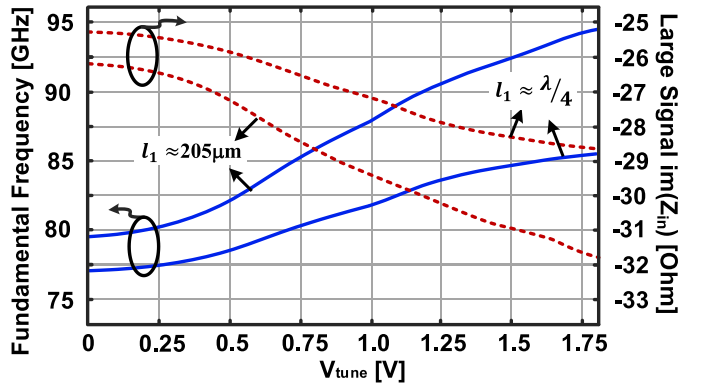
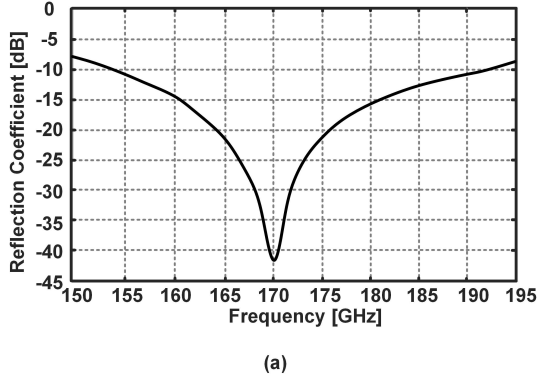


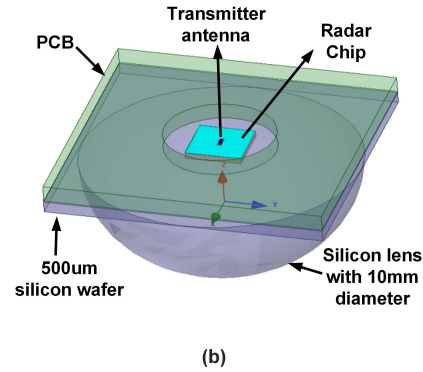
Fig. 6. Tuning range and the large signal input impedance at the base of Q_1 for $l_1 \approx \lambda/4$ and $l_1 = 205 \mu\text{m}$.

It is verified by the simulations that for $l_1 < l_{1,\text{opt}} = 180 \mu\text{m}$ the oscillation decays for $V_{\text{tune},\max} = 1.8 \text{ V}$, which was expected by theoretical analysis. In case of $l_1 < 180 \mu\text{m}$, the oscillation is not sustained for $V_{\text{tune},\max} = 1.8 \text{ V}$, therefore the maximum value of V_{tune} should be chosen less than 1.8 V in order to provide a capacitive impedance at the source, but the tuning bandwidth shrinks significantly, as shown in Fig. 5. In our design, in order to consider the process variations, a safe margin of 15% is assumed and an $l_1 = 205 \mu\text{m}$ is implemented, though, it is at the expense of losing $\sim 3 \text{ GHz}$ of the maximum achievable bandwidth. Based on the circuit simulations, for $l_1 = \lambda/4 \approx 420 \mu\text{m}$, a tuning range of 77–85.7 GHz (10.7%) at the fundamental frequency is achieved, as illustrated in Fig. 6. By implementation of $l_1 = 205 \mu\text{m}$, the tuning range increases to 79.1–94.3 GHz (17.5%), as shown in Fig. 6. The large signal input impedance looking in to the base of Q_1 is also simulated and illustrated in Fig. 6. As expected, variation of $I_m(Z_{\text{in}})$ is significantly larger in the proposed design which resulted in a wider tuning bandwidth of the VCO. Using this design technique, in [35], we have demonstrated a 220 GHz radiator with a state-of-the-art tuning bandwidth of 62 GHz (28.3%).

The common-node N_1 in the implemented structure of Fig. 2 ensures the differential oscillation of the structure. In this structure by reusing the dc current, the collector of



(a)



(b)

Fig. 7. Tx. antenna. (a) Simulated reflection coefficient of the slot antenna. (b) 3-D structure for EM simulation of the antenna. The transceiver chip is mounted on a $500\ \mu\text{m}$ silicon wafer, a silicon lens with 10 mm diameter is attached to the wafer, and the whole module is mounted on a metallized printed circuit board.

Q_1 is cascaded through Q_2 which buffers the resonance tank from the loading effect of the other parts. Transistor Q_3 acts as an active coupler to extract some portion of the power from the VCO to be injected to the Rx. side. Compared to a passive coupler, the active one has a smaller footprint and can boost the signal level. A quarter wavelength transformer at the second harmonic (T_6), diverts the second harmonic power toward the antenna. Implementation of VCO, buffer and the coupler in a single structure, decreases the silicon area, loss and the dc power consumption with no interstate mismatch concern.

Minimizing power variation across the bandwidth is critical for achieving the best imaging performance [27]. Variation of the generated power results in variation of both the radiated power (having an amplitude of V_{RF}) and the LO power (having an amplitude of V_{LO}) that is injected to the down-conversion mixer. Therefore, the IF signal level ($V_{IF} \propto V_{RF} \times V_{LO}$) is sensitive to the power variation. The variation of IF level across the band degrades the range resolution. A wide bandwidth design of the antenna and matching network is required to efficiently extract and radiate the generated second harmonic. Hence, a wideband slot antenna is implemented at the Tx. side. Besides, the feed of this antenna is single ended which is compatible with our power generation scheme. The output matching network and the slot gap size are optimized to provide more than 40 GHz of bandwidth. This covers the whole VCO bandwidth and tolerates the possible process variations. The reflection coefficient of the slot antenna is shown in Fig. 7(a). The matching network is designed to have the maximum radiated power at the center of the band. As a result, the variation of the radiated power across the band would be smaller and symmetric around the center frequency. To suppress the substrate modes, a high resistive hemispheric lens is assembled to the backside of the chip, as shown in Fig. 7(b). The simulated radiated power of the Tx. and its tuning range are illustrated in Fig. 8. In simulation, the Tx. radiates a peak power of $-0.5\ \text{dBm}$ with only 2.5 dB of variation across the bandwidth. The slot antenna is implemented on the top metal layer that is connected to the distributed ground plane, as shown in Fig. 9(a). A finger capacitor is used at the feed point for dc isolation of the antenna and the

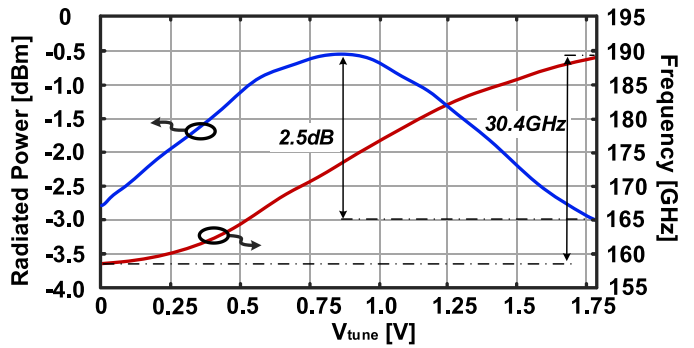


Fig. 8. Simulated tuning range and radiated power of the Tx.

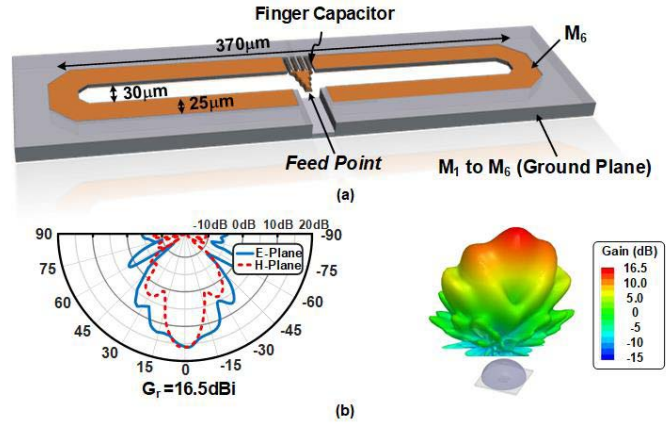


Fig. 9. Tx. antenna. (a) Dimension of the Tx. slot antenna. (b) Radiation pattern of the antenna.

supply. The simulated radiation pattern of the antenna with a gain of 16.5 dBi is shown in Fig. 9(b).

IV. RECEIVER FRONTEND

The extracted LO power by the couplers is at the fundamental frequency. Hence, by implementing a subharmonic mixer at the Rx., no frequency doubler is required [36]. The p-n junction of a bipolar transistor is used as the nonlinear element for RF down-conversion, as shown in Fig. 10(a). The

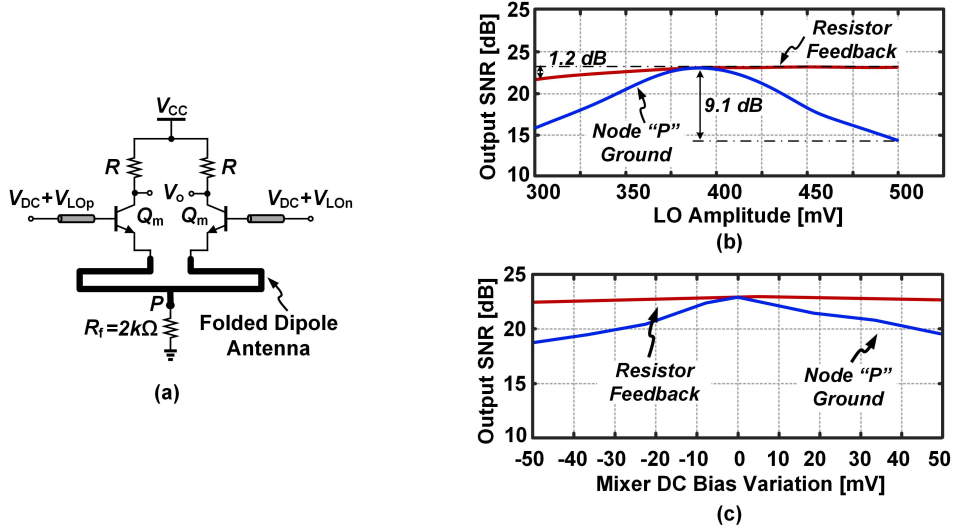


Fig. 10. Down-conversion mixer. (a) Subharmonic down-conversion mixer structure. (b) Output SNR variation due to variation of injected LO power. (c) Output SNR variation due to the bias variation.

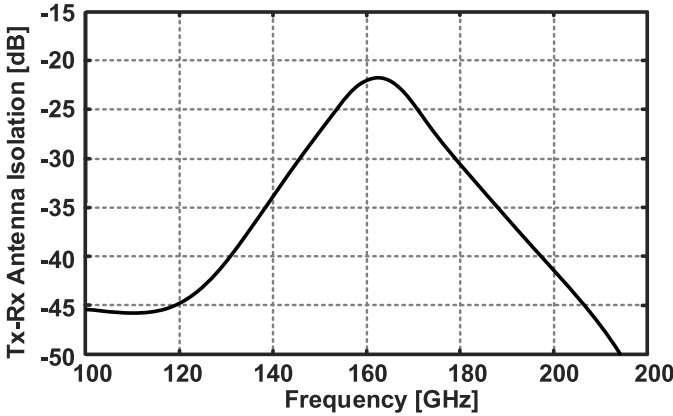


Fig. 11. Simulated isolation of the Tx.-Rx. antenna.

LO power is delivered to the base and the RF signal to the emitter via the Rx. antenna. To lower the sensitivity of the Rx. to the common-mode noises, a differential signal is preferred at the baseband. Therefore, at the Rx. side a dipole antenna is employed which provides a wide bandwidth response as well as a balanced signal. The folded dipole antenna is preferred over its dipole counterpart, since it offers $4\times$ larger input impedance [37]. It simplifies the matching networks of the Rx. antenna and the mixer. Co-design of the antenna and subharmonic mixer is utilized such that any extra matching network between the Rx. antenna and the mixer is not necessary. Consequently, the loss in the RF path is minimized. The nonlinearity of the bipolar transistor is governed by the voltage across the base-emitter junction. Hence, the conversion loss of the mixer is sensitive to the junction bias and the LO amplitude level. Based on the simulations, the injected LO amplitude at the mixer port varies from 300 to 500 mV. It degrades the output SNR by 9.1 dB across the band, as shown in Fig. 10(b). To overcome this issue a $2\text{k}\Omega$ resistor is placed at the middle point of the antenna (Node P) to ground. It provides

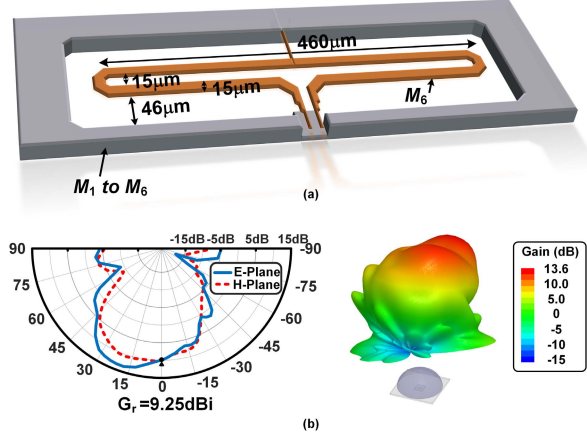


Fig. 12. Rx. antenna. (a) Dimension of the Rx. folded dipole antenna. (b) Pattern of the antenna.

a feedback loop and desensitize the performance from the variations. Adding this resistor stabilizes the operation region of Q_m and keeps this transistor in the active region while the LO amplitude is changing across the band. The node P is transparent for the balanced RF signal. Consequently, the Rx. performance is not degraded while variation of the SNR is limited to only 1.2 dB, as shown in Fig. 10(b). In addition, the sensitivity to dc bias of the mixer is significantly lowered, as illustrated in Fig. 10(c).

The polarization of the Tx. and Rx. antenna should be matched otherwise the received power level degrades. Considering the slot antenna is linearly vertically polarized, folded dipole antenna would be linearly horizontally polarized based on duality theorem [37]. Hence, Tx. and Rx. antennas should be implemented perpendicular. To minimize unwanted coupling of the Tx. and Rx. antennas and lower the leakage level, the dipole antenna is shielded at a distance of 46 μm by all the available metal layers. Nevertheless, there is still coupling through the substrate and near-field crosstalk of the

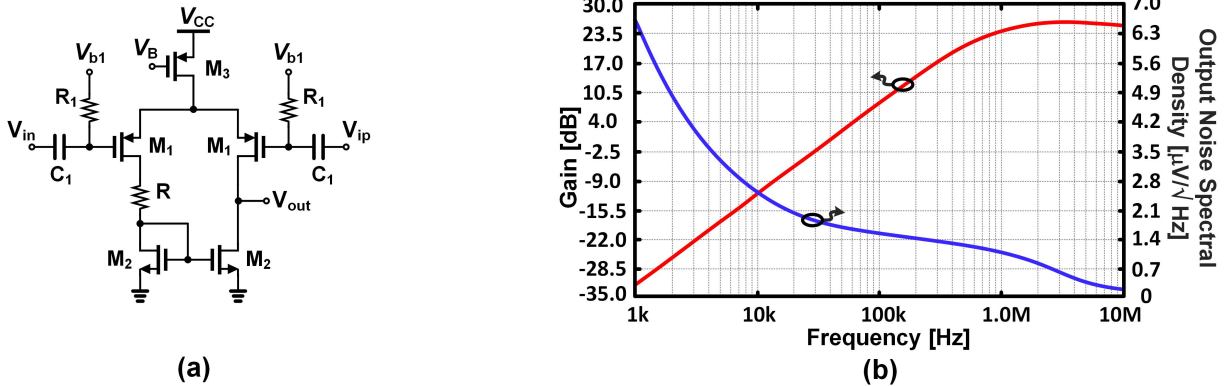


Fig. 13. LNA. (a) Structure of the implemented LNA. (b) Simulated performance of the LNA.

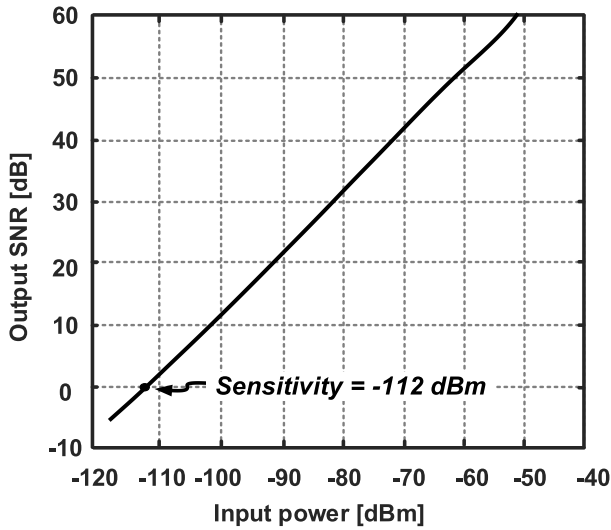


Fig. 14. Simulated output SNR of the Rx. chain versus the input power. It is used to calculate the sensitivity of the Rx.

antennas. The near-field coupling of the Tx.–Rx. antenna is simulated and shown in Fig. 11. Based on the EM simulations an isolation of better than -22 dB is expected, while it is -36 dB at the edge of the band. Given that the near-field coupling of the antennas only generates a dc component at the IF which is filtered by the high-pass filter of the following stages. The dimension of the Rx. antenna and its simulated radiation pattern are illustrated in Fig. 12(a). Bearing in mind that the Tx. antenna is at the center of silicon lens, the Rx. antenna will be off-axis. As a result, the beam of the Rx. is tilted [38], as shown in Fig. 12(b). It results in degradation of ~ 4 dB in gain of the Rx. antenna. Hence, a $G_r = 9.25$ dB at an incident angle of $\theta = 0$ is attained.

The differential IF signal is filtered and buffered through an on-chip differential to single-ended LNA and delivered to the pad. Implementation of an active RC-filter right after the mixer increases the input noise level of the Rx. frontend. Therefore, an LNA is implemented right after the mixer. The LNA structure is shown in Fig. 13(a). In this structure, the leakage is filtered by a first order high-pass filter to provide enough rejection of the leakage signal while making

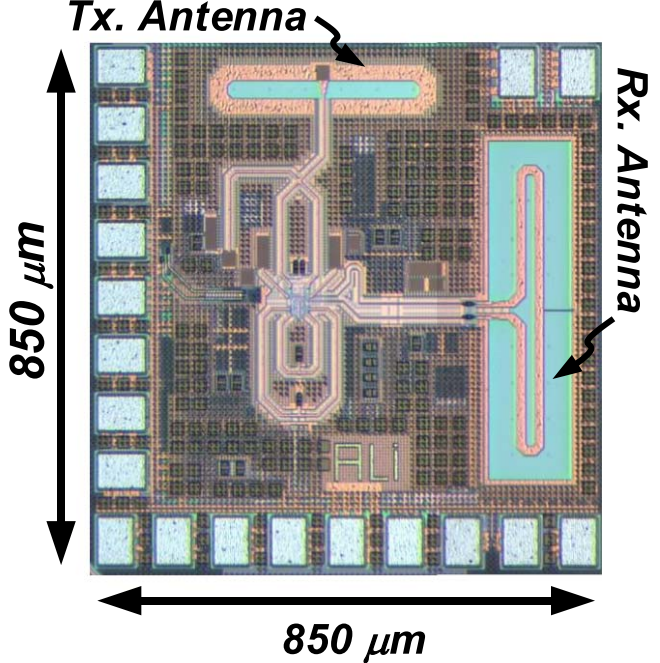


Fig. 15. Die micrograph of the fully integrated FMCW imaging radar.

sure that the LNA is not saturated. As we mentioned before, the leakage components are generated by the multi-reflection of the radiated wave at the si–air interface. Considering a chirp rate of 4 kHz, the first leakage component is generated at an IF frequency of 8 kHz, considering that the wave is propagated inside the 5 mm si-lens. In addition, based on the simulation result of Fig. 8, a maximum radiated power of ~ -0.5 dBm is expected. By considering that at the si–air interface almost 1/3rd of the power is reflected back (5-dB attenuation) a maximum incident power of no more than -5.5 dBm is expected at the Rx. antenna. Therefore, the cutoff frequency of the filter is chosen such that the LNA is not saturated for such signal at the Rx. antenna. It is noteworthy to mention that if a higher attenuation of the leaked signal at the IF is required, a high order sharp active RC filter can be implemented after the LNA to achieve higher rejection of the

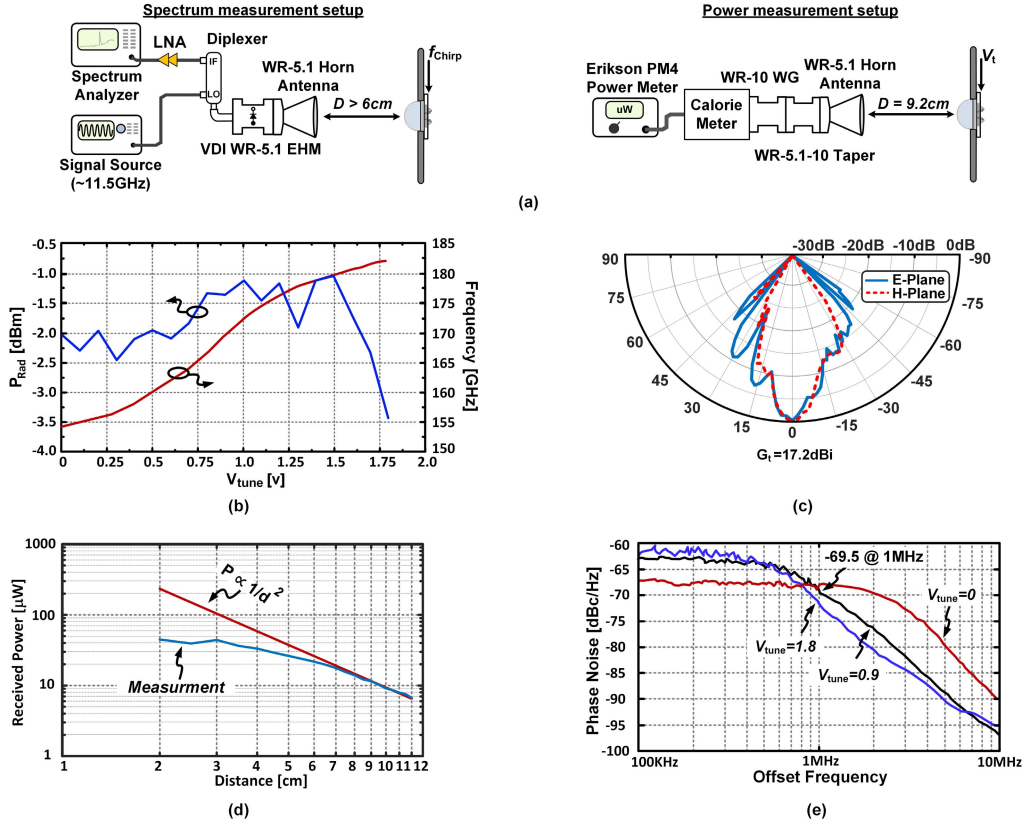


Fig. 16. Tx. measurement. (a) Spectrum and power measurement setup. (b) Measured tuning bandwidth and radiated power. (c) Measured radiation pattern. (d) Received power versus distance. (e) Measured phase noise of the VCO.

leakage while noise performance of the filter would not be a concern. The gain and the output noise spectral power density of the LNA are shown in Fig. 13(b). Based on the simulation result a total noise figure of 25.8 dB and a conversion gain of 42.5 dB with an almost flat response is achieved for the Rx. frontend. For a 4 kHz of bandwidth, the simulated output SNR versus the received power is shown in Fig. 14 which corresponds to a sensitivity of -112 dBm.

V. EXPERIMENTAL RESULTS

The imaging system is implemented in a $0.13\text{-}\mu\text{m}$ SiGe:BiCMOS process from STMicroelectronics. The chip micrograph is shown in Fig. 15 with a compact area of $0.72 \mu\text{m}^2$. As mentioned, the Tx. and Rx. antennas are implemented perpendicular to each other. This arrangement also compacts the design and shortens the LO to Rx. routing length.

A. Transmitter Measurement

The Tx. radiates through the substrate. Hence, to eliminate the lossy substrate waves, a high resistive hemispheric silicon lens is mounted on the backside of the chip. To ease the packaging, the chip is first mounted on a piece of silicon wafer with a thickness of $500 \mu\text{m}$. Then it is aligned to the center of the lens. Tx. measurement setup is shown in Fig. 16(a). Output spectrum is measured using VDI WR-5.1 EHM followed by a horn antenna. The radiated beam is mixed with the

14th harmonic of an 11.5 GHz source supplied by a signal generator. A measured radiation bandwidth of 154.5–182 GHz (27.5 GHz, 16%) is achieved, as shown in Fig. 16(b). By rotating the chip in both azimuth and elevation angles, the radiation pattern of the Tx. is measured and shown in Fig. 16(c). A directivity of 17.2 dBi is achieved that is in good agreement with EM simulations. The radiated power is measured using an Ericson PM4 calorimeter. To make sure far-field power measurements, colorimeter received power is measured over a distance of 2–12 cm. The received power is consistent with Friis equation for a far-field distance of 6.3 cm, as shown in Fig. 16(d). By measuring the received power at a far-field distance and using Friis equation the radiated power is calculated. The maximum radiated power and the EIRP are measured to be $790 \mu\text{W}$ and 16.2 dB, correspondingly. The VCO consumes 55.6 mW of power from a 2.6 V power supply. It results in a maximum dc to radiated power efficiency of 1.42% that is better than the state-of-the-art wideband VCO of [30]. Measured phase noise of the VCO for different tuning voltages is shown in Fig. 16(e). A phase noise level of -69.5 dBc/Hz at 1 MHz offset frequency at an oscillation frequency of 170 GHz is measured.

B. Receiver Measurement

Rx. measurement setup is shown in Fig. 17(a). A 4 kHz saw-tooth signal is applied to the VCO control voltage for frequency modulation to sweep the whole 27.5 GHz bandwidth.

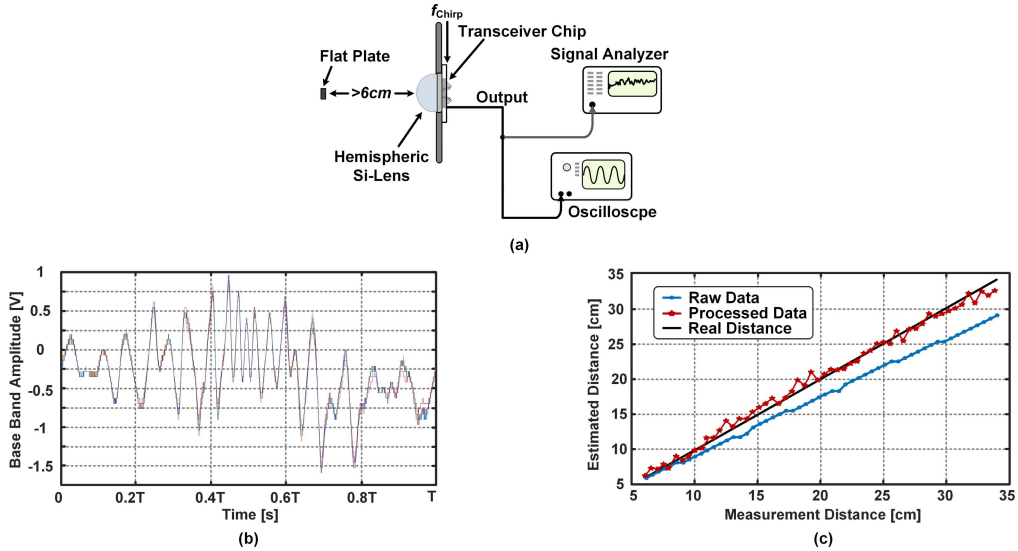


Fig. 17. Rx. measurement. (a) Rx. measurement setup. (b) Recorded baseband signal over time due to the leakage, $T = 1/4$ kHz is the chirp period. (c) Measured estimated flight distance.

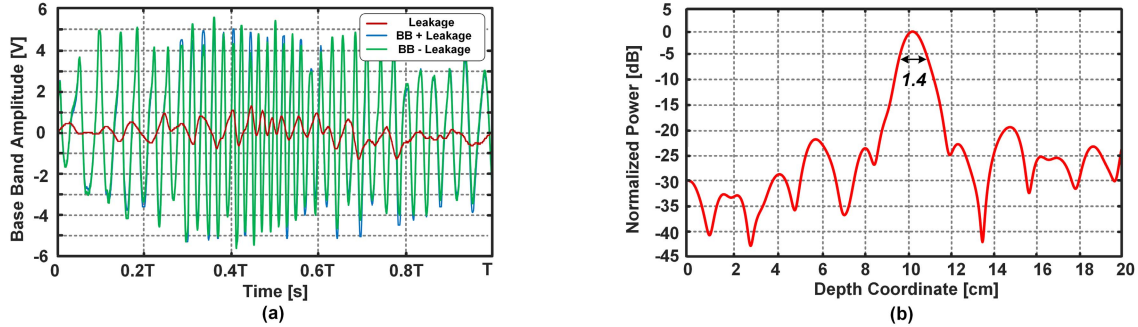


Fig. 18. Range resolution measurement results. (a) Baseband signal corresponding to a reflector plate at 10 cm distance, $T = 1/4$ kHz is the chirp period. (b) Processed range profile of a reflector at 10 cm distance with Hanning window.

However, the chirp sweep rate can be increased to 40 kHz. With no object in front of the imager, the IF signal is sampled which is generated by the Tx. to Rx. leakage. Transceiver is turned on and off ten times and the leakage signals within a chirp period (T) are recorded and shown in Fig. 17(b). As shown the IF signal is fixed over time. Therefore, in the calibration phase this residual leakage signal is stored and subtracted from all other IF signals in the presence of an object in front of the imager. It is noteworthy to mention that using a si-lens with impedance matching coating can significantly decrease the effect of multi-reflection and lowers the leakage level. The Rx. consumes 1.2 mW of power from a 1.8 V power supply which 0.3 mW of the power is dissipated in the detector and the rest in the LNA.

In order to measure the range estimation accuracy, a flat metal plate is placed in front of the imager at a distance of $R = 6$ cm and the system is calibrated. Then, the reflector is moved backward by 5 mm steps and the flight distance is estimated, as shown in Fig. 17(c). First, the flight distance is estimated just by calculating the fast Fourier transform (FFT) of the received signal with no further processing. An accuracy

of better than 8.8 mm at 11 cm distance is achieved. As the distance increases, due to the chirp nonlinearity, the accuracy of range estimation degrades. Next, the nonlinearity in the chirp frequency is corrected with post signal processing. Instead of uniform sampling of the IF signal, it is resampled and interpolated non-uniformly such that the IF signal is aligned in phase [26]. As shown in Fig. 17(c), the effect of the chirp nonlinearity in range estimation is significantly decreased with post processing. The standard deviation of the estimated flight distance from its correct value is 7.8 mm, which correspond to a range resolution of ~ 7.8 mm. It can also be verified by defining the main-lobe full-width at -6 dB of the IF spectrum as the range resolution. Therefore, a reflector is placed at a distance of 10 cm in front of the imager and the corresponding baseband signal is recorded and shown in Fig. 18(a). According to (2), a theoretical range resolution of 5.5 mm for 27.5 GHz of bandwidth is expected whereas a rectangular window is used in calculation of FFT. Rectangular window provides a sidelobe level of -13 dBc. In practice, usually Hamming/Hanning window is used which provides a sidelobe level of -43 dB/ -32 dB. As a result, the targets

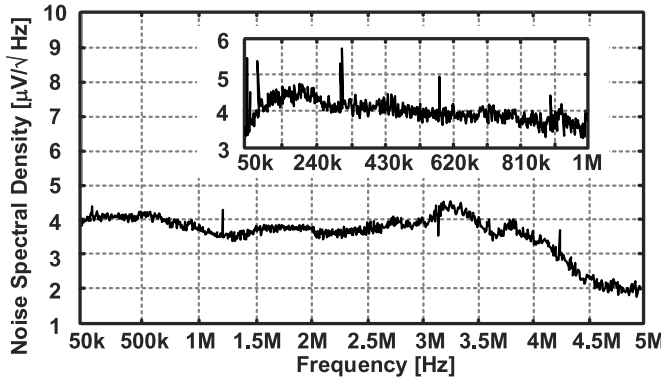


Fig. 19. Output noise power spectral density of the Rx.

TABLE II

MEASURED VALUES USED FOR CALCULATION OF THE SENSITIVITY

L	0.63	Silicon wafer losses
P_t	642 μW	Average transmitted power
G_t	17.2 dBi	Tx. antenna gain
G_r	9.25 dBi	Rx. antenna gain
σ	2.5 × 10⁻³ m²	Target radar cross section
λ	1.76 mm	Wavelength
R	6.3 cm	Distance to target
V_{rms,s}	195 mV	BB signal RMS value
V_n	4.3 μV/√Hz	Noise power density
BW	4 kHz	Band width

with small RCS can be detected in the vicinity of an object with large RCS. However, it widens the main-lobe width by a factor of 2. The processed range profile of the target at 10 cm distance is shown in Fig. 18(b). The main-lobe full-width at -6 dB is 14 mm for a Hanning window, corresponding to a range resolution of 7 mm which is in good agreement with the calculated value from standard deviation of the estimated distance.

Usually amplitude correction algorithms are also applied to enhance the range resolution even further. As illustrated in Fig. 18(a), an IF signal with an almost constant envelop is realized. Hence, in our design, the degradation of range resolution due to the amplitude variation is negligible. Therefore, no amplitude adjustment algorithms needs to be implemented, on the contrary to [16]. This simplifies the calibration of the imaging radar.

For coherent structures, the sensitivity can be measured by the difference between the received power and the output SNR. To measure the sensitivity, a 5 mm \times 5 mm flat metal plate is placed in the field of view of the imager at a distance of $R = 6.3$ cm. The RCS of a flat plate at a normal incident angle can be calculated by [39]

$$\sigma = 4\pi \frac{A^2}{\lambda^2} \quad (12)$$

where A is the area of the plate. The plate is carefully aligned to maximize the IF level. Using (1), a calculated received power of $P_r = -43.5$ dBm is expected. The values, which are used for calculation of, P_r are listed in Table II. Output SNR is calculated by

$$\text{SNR}_o = \frac{V_{\text{IF},\text{rms}}^2}{V_n^2 \times \text{BW}}. \quad (13)$$

The output noise power spectrum density of the Rx. is measured and shown in Fig. 19. As a result, $\text{SNR}_o = 57.1$ dB is expected referring to Table II. Finally, the sensitivity is calculated as

$$\text{Sensitivity} = P_r - \text{SNR}_o. \quad (14)$$

It results in a sensitivity of better than 87.3 fW.

C. Imaging Experiments

The imaging setup is shown in Fig. 20(a). A Teflon focal lens is used to focus the beam and achieve the lateral resolution. A stepper motor is used to scan the object in X - and Y -directions. A floppy disk is scanned by 1-mm steps in X - and Y -directions and the image is formed, as shown in Fig. 20(b). Because of the wave scattering at the edges and the high sensitivity of the imager any holes in the Floppy disk is clearly exposed. By performing range processing on the IF signal the depth information is extracted. As shown in the 3-D image of the floppy disk, the edges are exposed in the image that is due to the different scattering behaviors on the boundaries. To justify the functionality of the imager for sensing the water content of a target, an image of several water columns filled with water, is taken and illustrated. To verify the functionality of our imaging system for biomedical hydration sensing applications, a piece of meat is imaged. First, the image is taken while there is a piece of fat on the meat, then the fat is removed and the image is taken again. The images clearly show the different reflection behavior of the fat tissue compared to the meat. A 3-D image of an object (attenuator box) is taken which verifies functionality of the system for 3-D image formation. Note that except the 4-kHz saw-tooth signal (which can be easily implemented on the chip) no other external signal is required. Finally, in order to justify the stability of the radar operation over a long imaging acquisition time and verify the effectiveness and consistency of the leakage cancellation scheme, a key is raster scanned twice while an identical leakage signal is assumed for the two scans. The image is formed from 2600 pixels, as illustrated in Fig. 21, with a total acquisition time of 22 minutes. The imaging time is limited by the mechanical monuments. After 1 hour, the same key is imaged again, and then the two images are numerically compare by taking the difference of the two. As shown, the differential image has a much lower pixel intensity than the actual images. This justifies the radar operation over a long imaging acquisition process.

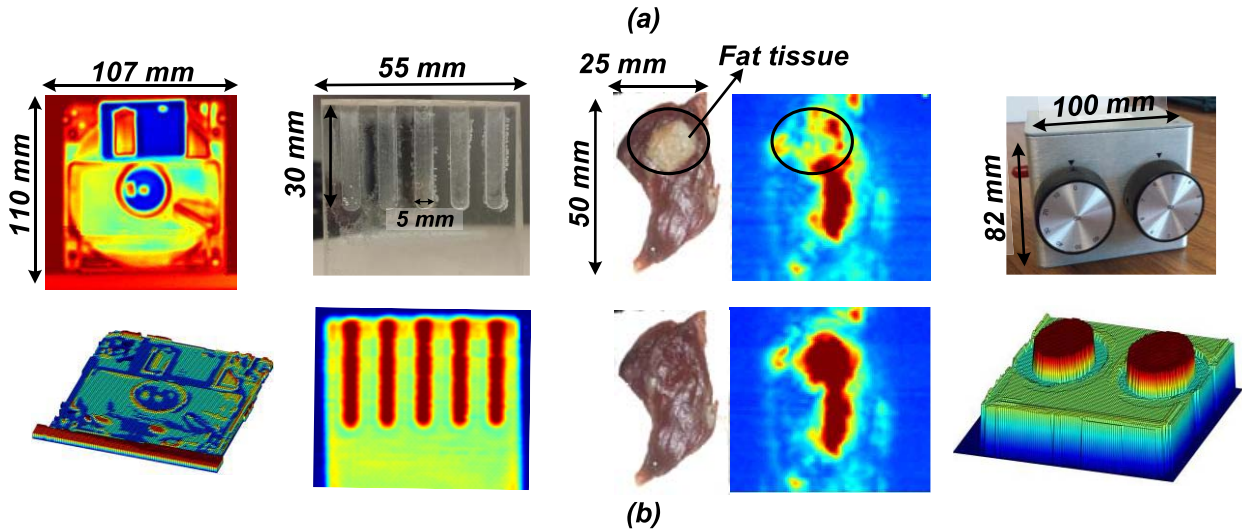
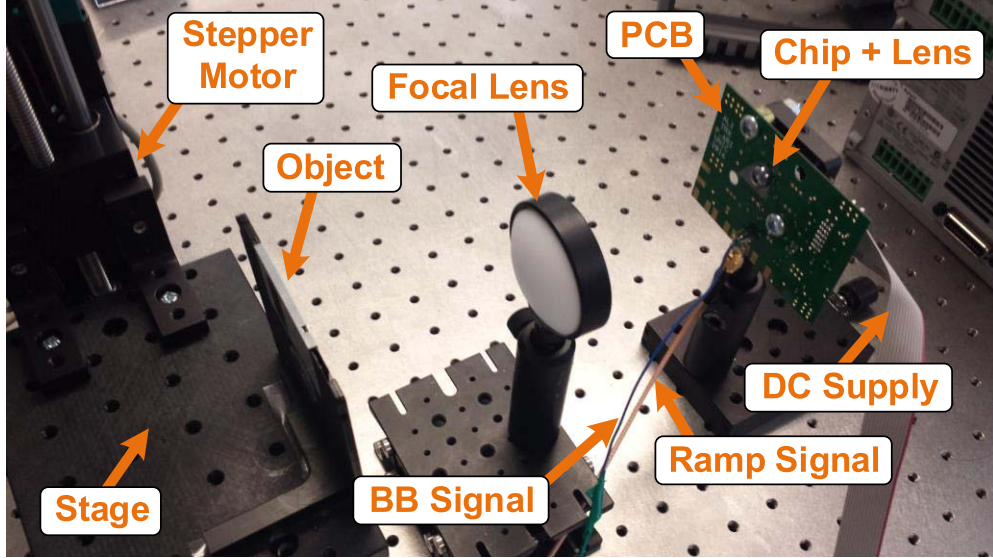


Fig. 20. Practical imaging with the radar. (a) Measurement setup. (b) 2-D and 3-D images of a floppy disk, 2-D image of a series of holes filled with water in a plastic frame, detection of fat tissue on a piece of meat, and the 3-D image of a metallic object constructed with the implemented FMCW imaging radar.

TABLE III
PERFORMANCE SUMMARY AND COMPARISON WITH STATE-OF-THE-ART IMAGING SYSTEMS

References	Technology	Frequency [GHz]	Bandwidth [GHz / %]	Radiated Power [μW] / EIRP [dBm]	DC/RF Eff. [%]	Sensitivity ¹	Total DC Power [mW] ⁷	Total Si Area [mm^2] ⁷	Fully Integrated	Imaging Technique	3D Imaging / Range Resolution
[7]	130 nm SiGe ^{2,3}	280.5	9.0 / 3.2 %	190 / 9.4	0.06	1 nW	180	6.9	Yes ⁵	Transmission	No
[8]	130 nm SiGe ⁴	527.5	17 / 3.2 %	1000 / 26	0.40	12.6 nW	2500	4.2	Yes	Transmission	No
[10]	130 nm SiGe ³	321	3.9 / 1.2 %	2030 / 21.1	0.41	70.1 pW	722	5.14	Yes	Transmission	No
[16]	130 nm SiGe ⁴	240	60 / 25 %	3160 / 31.6	0.16	NA	1800	3.2	No ⁶	FMCW	Yes/2.57mm
[17]	130 nm SiGe ⁴	227	40 / 17.6 %	500 / 30	NA	NA	3500	2.25	Yes ⁸	FMCW	Yes/3.8mm
This Work	130 nm SiGe ³	168.3	27.5 / 16.3%	790 / 16.2	1.42	87.3 fW	67	0.72	Yes	FMCW	Yes/7.0mm

¹ Calculated over 4kHz band width.

² Tx. is fabricated in 45nm CMOS $f_t / f_{\max} \approx 190\text{GHz}/220\text{GHz}$ and Rx. in 130nm SiGe.

³ $f_t / f_{\max} \approx 230\text{GHz}/280\text{GHz}$

⁴ $f_t / f_{\max} \approx 300\text{GHz}/450\text{GHz}$.

⁵ Lock-in amplifier is used for signal integration.

⁶ The chirp is generated off-chip at a frequency of 15GHz.

⁷ The total DC power consumption of the transmitter and receiver chips.

⁸ Some blocks of the PLL are implemented off-chip.

VI. CONCLUSION

In Table III, performance of the implemented FMCW imaging radar is summarized and compared with other state-of-the-art THz radiators in silicon. We presented a fully integrated ultralow power FMCW imaging radar that is

capable of practical 2-D and 3-D imaging. On the contrary to state-of-the-art FMCW radars that consumes a couple of watts of power our structure consumes only 64.7 mW of power in total that can be run with a battery. The compact design of the transceiver with a total area of 0.72 mm^2 makes the

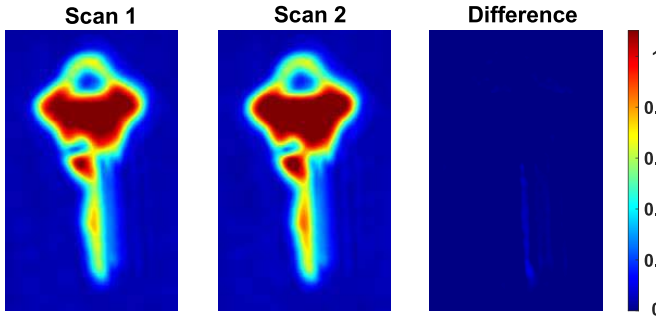


Fig. 21. A key is rescanned after 1 hour to show the stability of the radar operation. The difference of the two images is also illustrated.

system cost efficient. In this work, we exhibited the feasibility of low cost, low power and fully integrated silicon imaging instrumentation for future 2-D and 3-D practical imaging applications, such as biomedical hydration sensing, security screening and industrial quality control.

ACKNOWLEDGMENT

The authors would like to thank Dr. B. Ginsburg and Dr. S. Samala from Texas Instruments for their support and productive discussions.

REFERENCES

- [1] Z. D. Taylor *et al.*, “THz and mm-Wave sensing of corneal tissue water content: *In vivo* sensing and imaging results,” *IEEE Trans. THz Sci. Technol.*, vol. 5, no. 2, pp. 184–196, Mar. 2015.
- [2] R. M. Woodward *et al.*, “Terahertz pulse imaging in reflection geometry of human skin cancer and skin tissue,” *Phys. Med. Biol.*, vol. 47, no. 21, p. 3853, Oct. 2002.
- [3] W. L. Chan, J. Deibel, and D. M. Mittleman, “Imaging with terahertz radiation,” *Rep. Progr. Phys.*, vol. 70, no. 8, pp. 1325–1379, Jul. 2007.
- [4] H.-B. Liu, H. Zhong, N. Karpowicz, Y. Chen, and X.-C. Zhang, “Terahertz spectroscopy and imaging for defense and security applications,” *Proc. IEEE*, vol. 95, no. 8, pp. 1514–1527, Aug. 2007.
- [5] M. I. Skolnik, *Radar Handbook*. New York, NY, USA: McGraw-Hill, 1990.
- [6] K. B. Cooper *et al.*, “Penetrating 3-D imaging at 4- and 25-m range using a submillimeter-wave radar,” *IEEE Trans. Microw. Theory Techn.*, vol. 56, no. 12, pp. 2771–2778, Dec. 2008.
- [7] K. Sengupta *et al.*, “Silicon integrated 280 GHz imaging chipset with 4×4 SiGe receiver array and CMOS source,” *IEEE Trans. THz Sci. Technol.*, vol. 5, no. 3, pp. 427–437, May 2015.
- [8] U. R. Pfeiffer *et al.*, “A 0.53 THz reconfigurable source module with up to 1 mW radiated power for diffuse illumination in terahertz imaging applications,” *IEEE J. Solid-State Circuits*, vol. 49, no. 12, pp. 2938–2950, Dec. 2014.
- [9] R. Han *et al.*, “A 320 GHz phase-locked transmitter with 3.3 mW radiated power and 22.5 dBm EIRP for heterodyne THz imaging systems,” in *IEEE Int. Solid-State Circuits Conf. (ISSCC) Dig. Tech. Papers*, Feb. 2015, pp. 1–3.
- [10] C. Jiang *et al.*, “A 320 GHz subharmonic-mixing coherent imager in 0.13 μm SiGe BiCMOS,” in *IEEE Int. Solid-State Circuits Conf. (ISSCC) Dig. Tech. Papers*, Feb. 2016, pp. 432–434.
- [11] R. Han *et al.*, “280 GHz and 860 GHz image sensors using Schottky-barrier diodes in 0.13 μm digital CMOS,” in *IEEE Int. Solid-State Circuits Conf. (ISSCC) Dig. Tech. Papers*, Feb. 2012, pp. 254–256.
- [12] R. A. Hadi *et al.*, “A 1 k-pixel video camera for 0.7–1.1 terahertz imaging applications in 65 nm CMOS,” *IEEE J. Solid-State Circuits*, vol. 47, no. 12, pp. 2999–3012, Dec. 2012.
- [13] M. Uzunkol, O. D. Gurbuz, F. Golcuk, and G. M. Rebeiz, “A 0.32 THz SiGe 4×4 imaging array using high-efficiency on-chip antennas,” *IEEE J. Solid-State Circuits*, vol. 48, no. 9, pp. 2056–2066, Sep. 2013.
- [14] A. Arbabian, S. Callender, S. Kang, M. Rangwala, and A. M. Niknejad, “A 94 GHz mm-Wave-to-baseband pulsed-radar transceiver with applications in imaging and gesture recognition,” *IEEE J. Solid-State Circuits*, vol. 48, no. 4, pp. 1055–1071, Apr. 2013.
- [15] J.-D. Park, S. Kang, and A. M. Niknejad, “A 0.38 THz fully integrated transceiver utilizing a quadrature push-push harmonic circuitry in SiGe BiCMOS,” *IEEE J. Solid-State Circuits*, vol. 47, no. 10, pp. 2344–2354, Oct. 2012.
- [16] J. Grzyb, K. Statnikov, N. Sarmah, B. Heinemann, and U. R. Pfeiffer, “A 210–270-GHz circularly polarized FMCW radar with a single-lens-coupled SiGe HBT chip,” *IEEE Trans. THz Sci. Technol.*, vol. 6, no. 6, pp. 771–783, Nov. 2016.
- [17] S. Thomas, C. Bredendiek, T. Jaeschke, F. Vogelsang, and N. Pohl, “A compact, energy-efficient 240 GHz FMCW radar sensor with high modulation bandwidth,” in *Proc. German Microw. Conf.*, Mar. 2016, pp. 397–400.
- [18] Y. Tousi and E. Afshari, “A high-power and scalable 2-D phased array for terahertz CMOS integrated systems,” *IEEE J. Solid-State Circuits*, vol. 50, no. 2, pp. 597–609, Feb. 2015.
- [19] P.-Y. Chiang, O. Momeni, and P. Heydari, “A highly efficient 0.2 THz varactor-less VCO with -7 dBm output power in 130 nm SiGe,” in *Proc. IEEE CSICS Symp.*, Oct. 2012, pp. 1–4.
- [20] Y. M. Tousi, O. Momeni, and E. Afshari, “A novel CMOS high-power terahertz VCO based on coupled oscillators: Theory and implementation,” *IEEE J. Solid-State Circuits*, vol. 47, no. 12, pp. 3032–3042, Dec. 2012.
- [21] T. B. A. Senior, K. Sarabandi, and F. T. Ulaby, “Measuring and modeling the backscattering cross section of a leaf,” *Radio Sci.*, vol. 22, no. 6, pp. 1109–1116, Nov. 1987.
- [22] W. Wu, R. B. Staszewski, and J. R. Long, “A 56.4-to-63.4 GHz multi-rate all-digital fractional-N PLL for FMCW radar applications in 65 nm CMOS,” *IEEE J. Solid-State Circuits*, vol. 49, no. 5, pp. 1081–1096, May 2014.
- [23] Y. Zhao *et al.*, “A 0.56 THz phase-locked frequency synthesizer in 65 nm CMOS technology,” *IEEE J. Solid-State Circuits*, vol. 51, no. 12, pp. 3005–3019, Dec. 2016.
- [24] H. Mizutani, M. Tsuru, T. Matsuzaka, K. Choumei, K. Kawakami, and M. Miyazaki, “A millimeter-wave highly linear VCO MMIC with compact tuning voltage converter,” in *Proc. EuMC*, Sep. 2006, pp. 1755–1758.
- [25] S. Scheiblhofer, S. Schuster, and A. Stelzer, “Signal model and linearization for nonlinear chirps in FMCW Radar SAW-ID tag request,” *IEEE Trans. Microw. Theory Techn.*, vol. 54, no. 4, pp. 1477–1483, Jun. 2006.
- [26] A. Anghel, G. Vasile, R. Cacoveanu, C. Ioana, and S. Ciocchina, “Short-range wideband FMCW radar for millimetric displacement measurements,” *IEEE Trans. Geosci. Remote Sens.*, vol. 52, no. 9, pp. 5633–5642, Sep. 2014.
- [27] M. Mei, W. Tian, L. Yin, and T. Zeng, “Research on amplitude-phase error for LFM CW radar,” in *Proc. Int. Radar Conf. (IET)*, Oct. 2015, pp. 1–4.
- [28] A. G. Stove, “Linear FMCW radar techniques,” *IEE Proc. F Radar Signal Process.*, vol. 139, no. 5, pp. 343–350, Oct. 1992.
- [29] H. Aghasi and E. Afshari, “Design of broadband mm-Wave and THz frequency doublers,” in *Proc. 42nd Eur. Solid-State Circuits Conf.*, Sep. 2016, pp. 367–372.
- [30] R. Kananiyeh and O. Momeni, “A 190.5 GHz mode-switching VCO with 20.7% continuous tuning range and maximum power of -2.1 dBm in 0.13 μm BiCMOS,” in *IEEE Int. Solid-State Circuits Conf. (ISSCC) Dig. Tech. Papers*, Jan. 2016, pp. 46–47.
- [31] M. I. Skolnik, *Introduction to Radar Systems*, 3rd ed. New York, NY, USA: McGraw-Hill, 2002.
- [32] P.-Y. Chiang, Z. Wang, O. Momeni, and P. Heydari, “A silicon-based 0.3 THz frequency synthesizer with wide locking range,” *IEEE J. Solid-State Circuits*, vol. 49, no. 12, pp. 2951–2963, Dec. 2014.
- [33] N. Pohl, H.-M. Rein, T. Musch, K. Aufinger, and J. Hausner, “SiGe bipolar VCO with ultra-wide tuning range at 80 GHz center frequency,” *IEEE J. Solid-State Circuits*, vol. 44, no. 10, pp. 2655–2662, Oct. 2009.
- [34] P. R. Gray, *Models for Integrated-Circuit Active Devices*. New York, NY, USA: Wiley, 2001.
- [35] A. Mostajeran and E. Afshari, “An ultra-wideband harmonic radiator with a tuning range of 62 GHz (28.3%) at 220 GHz,” in *Proc. IEEE Radio Freq. Integr. Circuits Symp. (RFIC)*, Jun. 2017, pp. 164–167.
- [36] C. Jiang *et al.*, “A fully integrated 320 GHz coherent imaging transceiver in 130 nm SiGe BiCMOS,” *IEEE J. Solid-State Circuits*, vol. 51, no. 11, pp. 2596–2609, Nov. 2016.
- [37] C. Balanis, *Antenna Theory Analysis and Design*, 2nd ed. New York, NY, USA: Wiley, 1997.
- [38] A. V. Boriskin, G. Godi, R. Sauleau, and A. I. Nosich, “Small hemielliptic dielectric lens antenna analysis in 2-D: Boundary integral equations versus geometrical and physical optics,” *IEEE Trans. Antennas Propag.*, vol. 56, no. 2, pp. 485–492, Feb. 2008.
- [39] L. Tsang, J. A. Kong, and K. Ding, *Scattering of Electromagnetic Waves: Theories and Applications*. New York, NY, USA: Wiley, 2000.



Ali Mostajeran (S'15) received the B.Sc. degree in electrical engineering from the Isfahan University of Technology, Isfahan, Iran, in 2011, the M.Sc. degree in microelectronics from the Sharif University of Technology, Tehran, Iran, in 2013, and the M.Sc. degree in electrical and computer engineering from Cornell University, Ithaca, NY, USA, in 2016, where he is currently pursuing the Ph.D. degree.

He was with the Ultra-High-Speed Nonlinear Integrated Circuits Lab, Cornell University. In 2016, he joined the Radiation Laboratory, University of Michigan, Ann Arbor, MI, USA, as a Visiting Student. His current research interests include novel millimeter-wave and terahertz electronics for imaging, especially for biomedical hydration sensing applications.

Mr. Mostajeran was a recipient of the Sporck Analog Design Fellowship and Cornell graduate Fellowship, Cornell University, in 2013 and 2014. He is a member of the IEEE Solid-State Circuits Society, the IEEE Circuits and Systems Society, and the IEEE Microwave Theory and Techniques Society.



Ehsan Afshari (S'98–M'07–SM'11) was born in 1979. He received the B.Sc. degree in electronics engineering from the Sharif University of Technology, Tehran, Iran, and the M.S. and Ph.D. degrees in electrical engineering from the California Institute of Technology, Pasadena, CA, USA, in 2003 and 2006, respectively.

In 2006, he joined the faculty in electrical and computer engineering with Cornell University, Ithaca, NY, USA, as an Assistant Professor, and was promoted to Associate Professor in 2012. In 2016,

he joined the Electrical Engineering and Computer Science Department, University of Michigan, Ann Arbor, MI, USA, as an Associate Professor. His current research interests include millimeter-wave and terahertz electronics and low-noise integrated circuits for applications in communication systems, sensing, and biomedical devices.

Prof. Afshari serves as the Distinguished Lecturer of the IEEE Solid-State Circuits Society and a member of the Technical Program Committee of the IEEE Radio Frequency Integrated Circuits Symposium. He was the Chair of the IEEE Ithaca Section, the Chair of Cornell Highly Integrated Physical Systems, a member of the International Technical Committee at the IEEE Solid-State Circuit Conference, a member of the Analog Signal Processing Technical Committee of the IEEE Circuits and Systems Society, a member of the Technical Program Committee at the IEEE Custom Integrated Circuits Conference, and a member of the Technical Program Committee at the IEEE International Conference on Ultra-Wideband. He was a recipient of the National Science Foundation CAREER Award in 2010, the Cornell College of Engineering Michael Tien Excellence in Teaching Award in 2010, the Defense Advanced Research Projects Agency Young Faculty Award in 2008, and the Iran's Best Engineering Student Award by the President of Iran in 2001. He was also a recipient of the Best Paper Award at the Custom Integrated Circuits Conference, in 2003, the First Place at Stanford-Berkeley-Caltech Inventors Challenge, in 2005, the Best Undergraduate Paper Award at the Iranian Conference on Electrical Engineering, in 1999, the Silver Medal in the Physics Olympiad in 1997, and the Award of Excellence in Engineering Education from the Association of Professors and Scholars of Iranian Heritage, in 2004.



Andreia Cathelin (M'04–SM'11) started the Electrical Engineering degree with the Polytechnic Institute of Bucharest, Romania and continued and received the Degree from the Institut Supérieur d'Électronique du Nord, Lille, France, in 1994. She received the Ph.D. and the *habilitation à diriger des recherches* (French highest academic degree) degrees from the Université de Lille 1, Villeneuve-d'Ascq, France, in 1998 and 2013, respectively.

Since 1998, she has been with STMicroelectronics, Crolles, France, and currently as a Fellow of Technology Research and Development. Her current research interests include RF/millimeter-wave/terahertz systems for communications and imaging. She has authored or co-authored more than 100 technical papers and four book chapters, and has filed over 25 patents. Dr. Cathelin is serving on several IEEE conferences and committees. She has been active at ISSCC since 2011. In 2011, she was a TPC Member, the RF Sub-Committee Chair from 2012 to 2015, and is currently the Forums Chair and a member of the Executive Committee. She has been a member of several technical program committees: VLSI Symposium on Circuits from 2010 to 2016, and ESSCIRC since 2005. Since 2013, she has been on the Steering Committee of the ESSCIRC-ESSDERC conferences, currently serving as Chair. She was a co-recipient of the ISSCC 2012 Jan Van Vessem Award for Outstanding European Paper and the ISSCC 2013 Jack Kilby Award for Outstanding Student Paper, as well as the Winner of the 2012 STMicroelectronics Technology Council Innovation Prize. She is an Elected Member of the IEEE SSCS Adcom from 2015 to 2017, and an active member of the SSCS Women in Engineering group.